Research Article **Open Access**

A. Sundar Rajan, M. K. Ravikumar, K. R. Priolkar, S. Sampath, and A. K. Shukla*

Carbonyl-Iron Electrodes for Rechargeable-Iron Batteries.

Abstract: Nickel-iron and iron-air batteries are attractive for large-scale-electrical-energy storage because iron is abundant, low-cost and non-toxic. However, these batteries suffer from poor charge acceptance due to hydrogen evolution during charging. In this study, we have demonstrated iron electrodes prepared from carbonyl iron powder (CIP) that are capable of delivering a specific discharge capacity of about 400 mAh g^{-1} at a current density of 100 mA g^{-1} with a faradaic efficiency of about 80%. The specific capacity of the electrodes increases gradually during formation cycles and reaches a maximum in the 180^{th} cycle. The slow increase in the specific capacity is attributed to the low surface area and limited porosity of the pristine CIP. Evolution of charge potential profiles is investigated to understand the extent of charge acceptance during formation cycles. *In situ* XRD pattern for the electrodes subsequent to 300 charge/discharge cycles confirms the presence of Fe with $Fe(OH)_2$ as dominant phase.

Keywords: Carbonyl iron electrodes, specific capacity, formation cycles, overpotential, potential overshoot

DOI 10.1515/eetech-2014-0002
Received October 29, 2014; revised December 15, 2014; accepted December 16, 2014

1 Introduction

Large-scale-electrical-energy-storage systems are necessary for integrating energy generated from solar and wind resources into the electricity grid. Iron-based rechargeable batteries are attractive for large-scale battery-based electrical-energy storage because iron is low-cost, globally abundant and environmentally friendly. Iron-based batteries are more preferred because they have higher theoretical specific capacity compared to systems like Pb-acid and are free from the problem of dendrite formation compared to $Li/LiMn_2O_4$, Zn/NiOOH, and $Zn/Na_{0.95}MnO_2$. Albeit these advantages, the commercial use of iron-based batteries remains limited due to their poor charge-acceptance brought about by hydrogen evolution and poor discharge-rate-capability of the iron electrodes [1–9].

Iron electrodes have two steps of charge and discharge reactions. The first step of charge/discharge reactions for the iron electrode is:

$$\begin{aligned} &Fe(OH)_2 + 2e^- \rightleftharpoons Fe + 2OH^- \\ &E \text{ vs. } Hg/HgO,\ OH^-(6M\ KOH) = -0.975\ V \end{aligned} \quad (1)$$

The redox process during first step of charge and discharge involves iron(II)hydroxide and elemental iron. During the second step of discharge the ferrous hydroxide is further oxidized to passive ferric hydroxide. Hence, Fe electrodes are subjected to only first step of charge and discharge cycles. Theoretical specific-capacity for Fe electrode is 960 mAh g^{-1} for the first step of discharge reaction. Since the redox potential for iron-electrode reaction is cathodic to the hydrogen-evolution potential, iron electrode is thermodynamically susceptible to parasitic hydrogen-evolution reaction during its charge [10–12]. Hence, Fe electrodes exhibit low specific capacity. In the literature [13–21], it is established that overpotential for hydrogen-evolution reaction can be increased by using certain additives, namely FeS, PbS and Bi_2S_3. The discharge product for iron-electrode reaction is $Fe(OH)_2$ which is an insulating material that could passivate the electrode. To mitigate this problem, Fe/C composite electrodes with improved conductivity are reported in the literature [22–27].

Carbon-grafted-iron electrodes exhibit good discharge rate capabilities [28, 29]. However, the synthesis of carbon-grafted-iron material requires distinctive arrangements both for its production and storage. Alternatively, we have made an attempt to utilize a commercially available carbonyl iron powder (BASF, Germany) as active material to examine its suitability for alkaline-iron electrodes. In

***Corresponding Author: A. K. Shukla:** Solid State and Structural Chemistry Unit, Indian Institute of Science, Bangalore-560012, India Email: akshukla2006@gmail.com.
A. Sundar Rajan, M. K. Ravikumar: Solid State and Structural Chemistry Unit, Indian Institute of Science, Bangalore-560012, India
K. R. Priolkar: Department of Physics, Goa University, Taleigao Plateau, Goa-403206, India
S. Sampath: Inorganic and Physical Chemistry Department, Indian Institute of Science, Bangalore-560012, India

this study, we report the characterization of CIP by XRD, XPS, EXAFS and XANES in conjunction with electrochemical measurements. Carbonyl iron electrode exhibits specific discharge-capacity of 400 mAh g^{-1} during the first step of discharge with a faradaic efficiency of 80%. Ironically, however, the specific capacity of these electrodes increases slowly over several charge/discharge cycles, reaches a maximum in the 180th cycle and declines slowly during the subsequent cycles. The reason for slow increase in the specific capacity of the carbonyl iron electrodes is the low surface area of CIP. Charge potential profiles during formation cycles for the carbonyl iron electrodes are examined to understand the extent of iron-electrode reaction ($Fe(OH)_2$/Fe) in relation to the parasitic hydrogen-evolution-reaction. *In situ* electrochemical X-ray diffraction analysis of the charged and discharged electrodes after 300 cycles shows the presence of metallic iron and $Fe(OH)_2$.

2 Methods

Electrochemical Characterization

Iron electrodes employed in the study comprised 82.5 wt.% carbonyl iron powder (BASF, Germany), 10 wt.% graphite powder, 1 wt.% Bi_2S_3 and 0.5 wt.% $NiSO_4 \cdot 7H_2O$. These materials were added to 3 wt.% KOH solution and mixed homogeneously to form a slurry to which 6 wt.% polytetrafluoroethylene (PTFE, 60 wt.% dispersion in H_2O) was added. After adding PTFE to the slurry, a dough was formed which was spread onto a degreased nickel mesh of dimensions 3.1 cm × 3.3 cm followed by compaction at 675 kg cm^{-2}. The compacted electrodes were sintered at 350°C in nitrogen atmosphere. About 1.25 g of CIP was distributed over an area of 17.4 cm^2 providing active material loading of 72 mg cm^{-2} in the electrode. The iron electrodes were tested in a three-electrode electrochemical cell with nickel oxyhydroxide counter electrodes on either side with mercury/mercuric oxide (MMO in 6 M KOH) as the reference electrode (E°_{MMO} = 0.098 V *vs.* SHE). 6 M aqueous KOH solution with 1 w/v% LiOH was used as the electrolyte. Galvanostatic charge/discharge and potentiostatic polarization experiments were performed using a Solartron analytical cell test system (Model 1470E, AMETEK, UK). Steady-state potentiostatic polarization measurements were conducted for a charged iron electrode in the potential range between −1.2 V and −0.8 V *vs.* MMO by stepping the electrode potential in 10 mV steps and holding the potential for 300 s before recording the steady-state current.

X-ray diffraction characterization

Powder X-ray diffraction (XRD) pattern for CIP and *in situ* electrochemical (EC) XRD patterns for carbonyl iron electrodes were recorded on a Bruker D8 Discover X-ray diffractometer using Co source (λ = 1.78897 Å). *In situ* electrochemical X-ray diffraction patterns for carbonyl iron electrodes were recorded using a 3-electrode electrochemical cell developed in-house.

Scanning electron microscopic characterization

Field Emission Scanning Electron Microscope (FESEM, Sirion FEI, USA) was used to characterize morphology of CIP.

X-ray photoelectron spectroscopic characterization

An X-ray photoelectron spectroscopic (XPS) measurement was carried out on the CIP using Thermo-Fischer Multilab 2000 instrument with MgK_{α} X-ray source.

XANES and EXAFS characterization

XANES and EXAFS spectra for CIP and Fe metal powders were recorded using scanning EXAFS beamline (BL 9) at INDUS-II Synchrotron source (India) in transmission mode using absorbers made from finely ground powder uniformly distributed on a scotch tape. Such sample coated strips were adjusted in number such that the absorption edge jump gave $\Delta\mu t \leq 1$ where $\Delta\mu$ is the change in absorption coefficient at the absorption edge and t is the thickness of the absorber. The incident and transmitted photon energies were simultaneously recorded using gas-ionization chambers as detectors. Measurements were carried out from 200 eV below the edge energy to 800 eV above it. Data analysis was carried out using Demeter analysis program [30]. Here theoretical fitting standards were computed with FEFF6 [31]. The data in the k range of 3 – 12 $Å^{-1}$ and R range of 1 – 3 Å were used for analysis.

3 Results and Discussion

Powder XRD pattern for the CIP and *in situ* EC XRD patterns for the carbonyl iron electrode in charged and discharged

state after 300 cycles are recorded and presented in Figures 1(a) – 1(c). Powder XRD pattern for CIP shown in Figure 1(a) exhibits three diffraction peaks at 2θ values 52.36°, 77.22° and 99.70°, which correspond to (110), (200) and (211) planes of the α-Fe in body-centered-cubic-crystal system. Figures 1(b) and 1(c) show the *in situ* EC XRD patterns for carbonyl iron electrode in charged and discharged states, respectively, after 300 cycles. All XRD patterns were background subtracted and noise corrected. The electrode exhibits mixed phases of α-Fe, $Fe(OH)_2$ and the carbon additive used during the preparation of electrodes. It is also observed that there are few additional peaks marked with (*). The intensities of these peaks do not show any significant change in charged and discharged state indicating that these are most likely due to passive iron oxides formed during 300 charge/discharge cycles. The data suggest the presence of $Fe(OH)_2$ in hexagonal crystal system. The intensity of these peaks increases in discharged electrode compared to charged electrode suggesting that the product formed during the first step of discharge reaction is mainly $Fe(OH)_2$ as represented in Eqn. 1. *In situ* EC XRD data for electrodes after 300 charge/discharge cycles show the presence of $Fe(OH)_2$ as dominant phase and likely being primarily responsible for the decay in electrode capacity. Figure 2 shows the FESEM images of CIP with spherical particles of 2 – 5 micron size. Figure 3 shows Fe $2p_{3/2}$ XPS spectra for CIP. The spectrum is recorded in the region 702.5 – 717 eV and is deconvoluted using XPSPEAK 4.1 software. In the spectrum, the Fe(0)-$2p_{3/2}$ peak observed at 706.8 eV is characteristic of metallic iron while Fe(II)-$2p_{3/2}$ peaks at 708.4 eV and 709.2 eV are characteristic of Fe(II) in Fe_3O_4; Fe(III)-$2p_{3/2}$ peaks observed at 710.2 eV, 711.2 eV, 712.3 eV, 713.4 eV and 714.5 eV correspond to Fe(III) in Fe_3O_4. The spectrum is fitted using Fe $2p_{3/2}$ spectral fitting parameters from the literature [32]. The area under the respective peaks corresponds to the amount of metallic iron and Fe_3O_4 present on the surface of the sample. The amount of metallic iron present on the surface of the CIP is about 66% and the rest is magnetite. While Fe $2p_{3/2}$ XPS spectra indicated the presence of about 34% of Fe_3O_4 in CIP, XRD data did not show presence of Fe_3O_4. This could be due to the fact that XPS, unlike XRD, is a surface analytical technique. In order to ascertain the bulk nature of the CIP, Fe K edge XANES and EXAFS transmission spectra for both the CIP and metallic iron were recorded. These results are presented in Figure 4 and Figure 5(a) and 5(b). A plot of normalized Fe K edge in CIP sample is presented along with Fe metal in the Figure 4. It can be seen that the Fe K edge in CIP closely resembles that in Fe metal. All the XANES features seen in Fe metal can be clearly seen in CIP. There is no chemical shift present between CIP and

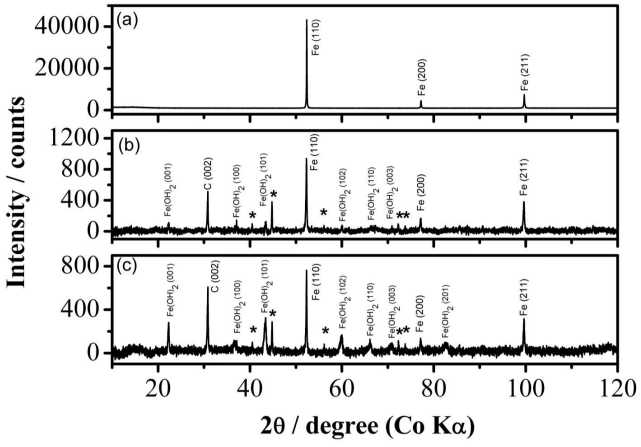

Figure 1: (a) Powder XRD pattern for carbonyl iron powder, (b) *in situ* electrochemical XRD pattern for the carbonyl iron electrode in charged and (c) in discharged states (International Centre for Diffraction Data (ICDD) number for α-Fe, $Fe(OH)_2$ and graphitic carbon are 00-006-0696, 00-013-0089 and 00-041-1487, respectively).

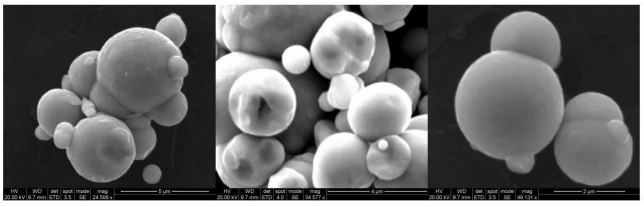

Figure 2: FESEM images for carbonyl iron powder.

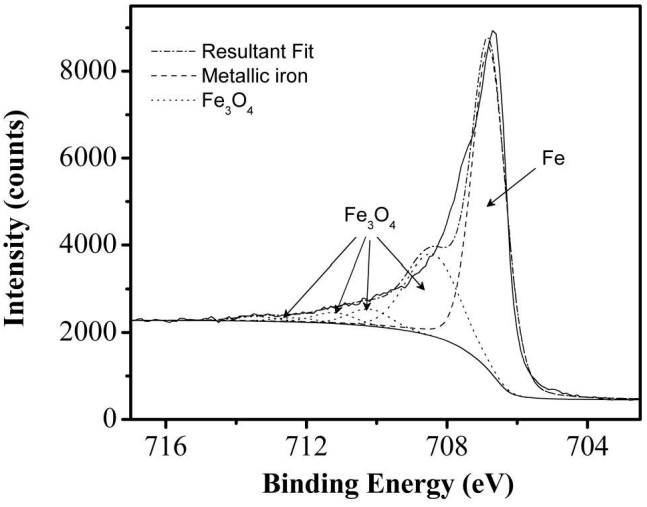

Figure 3: Fe $2p_{3/2}$ XPS spectra for carbonyl iron powder.

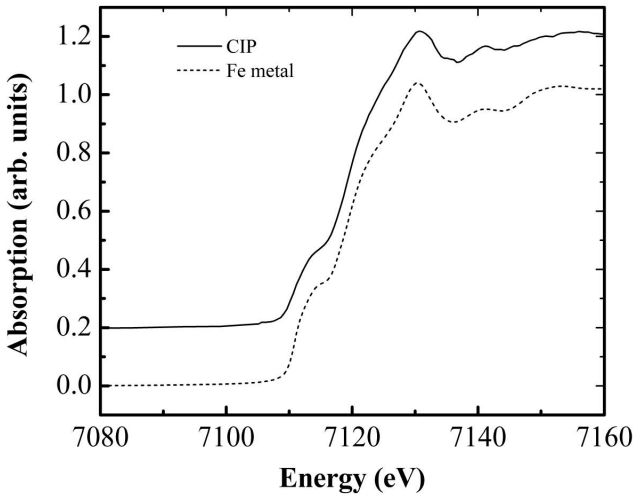

Figure 4: XANES spectra for carbonyl iron powder and Fe metal.

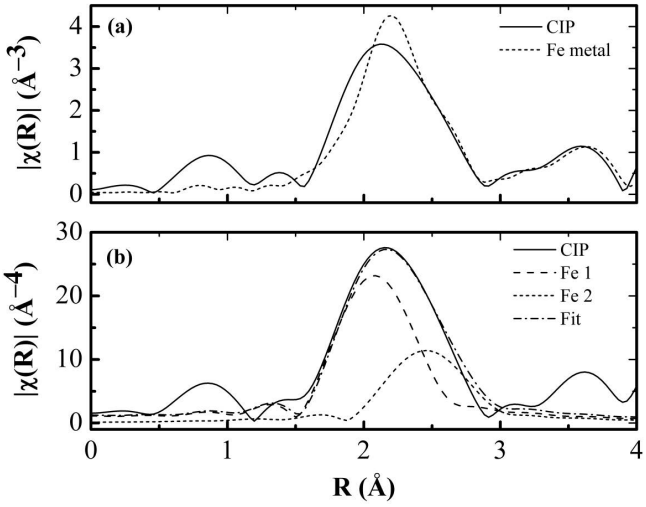

Figure 5: (a) EXAFS spectra for carbonyl iron powder and Fe metal (b) fitted EXAFS spectra for carbonyl iron powder.

Fe metal. In this case the edge position was determined as first maximum in derivative spectra. This indicates that Fe in CIP is in Fe^0 state.

EXAFS data shown in Figure 5(a) and 5(b) also agrees with the above. The magnitude of Fourier Transform (FT) of Fe K EXAFS spectra in CIP could be fitted purely with Fe-Fe correlations belonging to Fe metal is presented in Figure 5(b). In Figure 5(a), FT magnitude in CIP is compared with Fe metal. The similarities between the magnitudes of FT spectra in Figure 5(a) confirm that the local structural environment around Fe in CIP is akin to Fe metal. A fit to the spectra in the range 1 Å to 3 Å using Fe-Fe correlations yields structural parameters shown in Table 1. It is noteworthy that the fitting parameters show Fe is present in two different environments, namely one with 6 Fe neighbours at 2.805 Å bond distance and the other with 8 Fe neighbours at little shorter distance of 2.429 Å.

Table 1: EXAFS fitting parameters for CIP.

Bond	Bond length R(Å)	σ^2 (Å^2)	N*	E_0 (eV)
Fe-Fe	2.429 (9)	0.004(1)	8	4.9(2)
Fe-Fe	2. 805 (9)	0.005(2)	6	4.9(2)

*Not varied while fitting.

On comparing XANES and EXAFS spectra for both Fe metal and CIP, there is hardly any evidence for the presence of either of iron oxides. Both clearly show that it is almost entirely iron metal. The XANES spectrum for CIP sample shows a small pre-edge peak that could be due to a transition from 1s to 3d. But this transition can be made allowed either due to hybridization of ligand p-orbitals like in case of iron oxides or due to quadrupole transition. Accordingly, iron metal also shows a pre-edge peak. Furthermore, if there was Fe_3O_4 or any other iron oxide, the Fe-O correlation at about 1.5 Å should have been observed since phase-corrected Fe-O distance is typically 1.9 Å. Such a correlation is not at all observed in CIP sample. Since XANES and EXAFS spectra do not show presence of any iron oxides, Fe_3O_4 observed in Fe $2p_{3/2}$ XPS spectra is assigned to surface oxide present in CIP.

Figure 6 shows the specific discharge capacity for carbonyl iron electrode as a function of cycle number. The specific capacity of the electrode increases gradually with cycle number. The electrochemically active surface area for the CIP increases progressively during charge/discharge cycling resulting from the gradual penetration of electrolyte into the inner core of particles [33]. These electrodes were charged and discharged at a current density of 100 mA g^{-1}. The specific capacity reaches a maximum of about 400 mAh g^{-1} with a faradaic efficiency of about 80% in 180th cycle. The slow increase in the specific capacity of the carbonyl iron electrode is due to the low surface area (~0.4 m^2 g^{-1}) and lesser porosity of CIP. The gradual capacity fade after 180 cycles is attributed to the formation of a passive layer on the electrodes as reflected in their *in situ* XRD patterns recorded after 300 cycles in charged and discharged states. Figure 7 shows the charge-potential profile for carbonyl iron electrodes in cycle number 2, 10, 40, 80, 120, 160 and 180 at a current density of 100 mA g^{-1}. A two potential plateau sequence is observed while charging the electrodes with the plateau potential varying with cycle number. The first potential plateau cor-

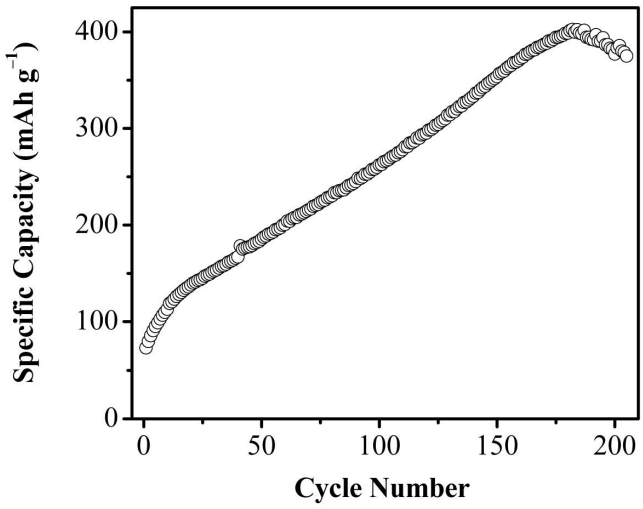

Figure 6: Specific discharge capacities for carbonyl iron electrode as a function of cycle number at a current density of 100 mA g^{-1}.

responds to the reduction of $Fe(OH)_2$ to Fe, while the second potential plateau is due to the hydrogen evolution reaction (HER) on the surface of metallic iron. An inflection region is observed between the first and second potential plateau which is shifted towards higher capacity with cycle number. Two distinct potential plateaus are observed from

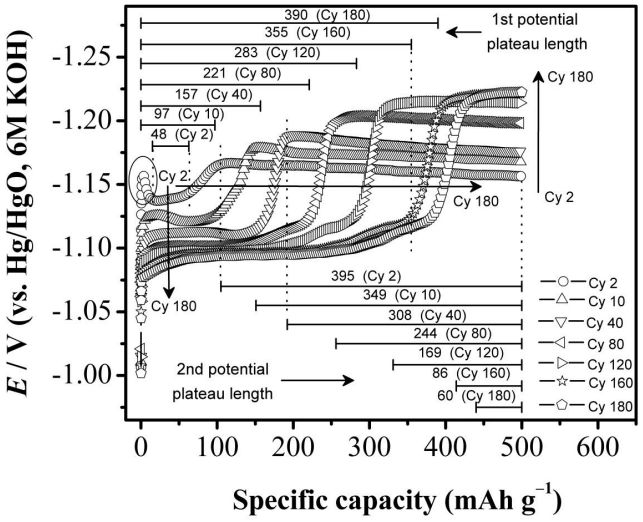

Figure 7: Charge potential profiles for carbonyl iron electrode in cycle number 2, 10, 40, 80, 120, 160 and 180 at a current density of 100 mA g^{-1}. The lengths (in mAh g^{-1}) of the first and second potential plateaus are indicated in the figure.

cycle 2 onwards. There are two noticeable features for the potential plateaus in the charge potential profiles, namely potentials at which the two plateaus appear and the length of the each potential plateau. In the 2nd cycle, the first potential plateau is observed at –1.138 V *vs.* MMO which is shifted towards lesser negative potential as the formation cycles proceed. In 20th, 80th, 120th and 180th cycle, the first potential plateau is observed at –1.117 V, –1.102 V, –1.097 V and –1.094 V *vs.* MMO which implies that the overpotential for the reduction of $Fe(OH)_2$ decreases as the formation proceeds. In 2nd cycle, conversion of $Fe(OH)_2$ to Fe occurs at higher overpotential of about –164 mV and upon further cycling, this reaction occurs at lesser overpotential of about –142 mV, –127 mV, –122 mV and –119 mV during 20th, 80th, 120th and 180th cycle. The change in the overpotential for the reduction of $Fe(OH)_2$ during the formation cycles is shown in Figure 8.

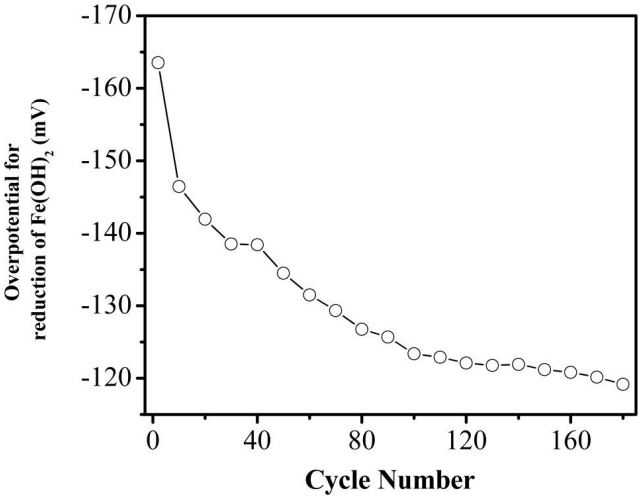

Figure 8: Change in the overpotential for the reduction of $Fe(OH)_2$ to Fe during the formation cycle.

The second potential plateau is observed at –1.156 V *vs.* MMO in the 2nd cycle. Up on further charge/discharge cycling, it is shifted towards more negative potential. During 20th, 80th, 120th and 180th cycle, the second potential plateau appears at –1.169 V, –1.198 V, –1.214 V and –1.223 V *vs.* MMO. This shows that the overpotential for the HER increases as the formation proceeds. In 2nd cycle, HER occurs at lesser overpotential of about –230 mV and during further charge/discharge cycles, HER occurs at higher overpotential of about –243 mV, –272 mV, –288 mV and –297 mV during 20th, 80th, 120th and 180th cycles. This is because the elemental Bi present in the electrode comes in contact with the newly exposed surface of the metallic iron as the formation cycle proceeds and increases the overpotential for HER [34, 35].

$$Bi_2S_3 + 6e^- \rightleftharpoons 2Bi + 3S^{2-} \qquad E^\circ = -0.818 \text{ V vs. SHE} \tag{2}$$

The change in the overpotential for the HER during formation cycles is shown in Figure 9.

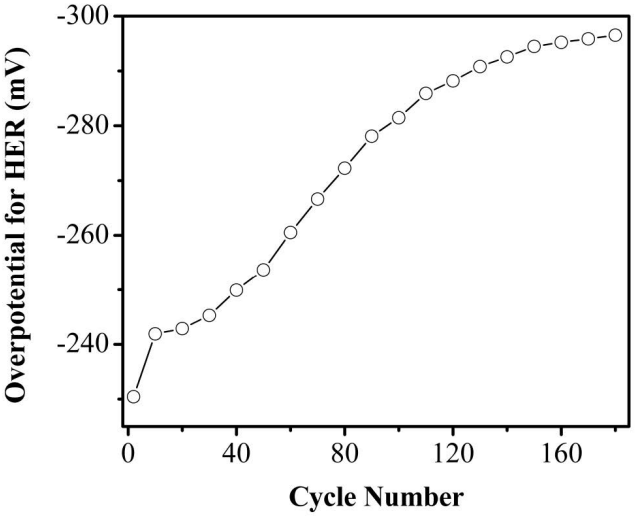

Figure 9: Change in the overpotential for the HER during the formation cycle.

Since first potential plateau corresponds to reduction of $Fe(OH)_2$ to α-Fe and second to the HER, charge acceptance of the electrode can be directly related to the length (in mAh g^{-1}) of the first potential plateau. Accordingly, longer the first potential plateau, higher will be the charge acceptance for the electrode. Similarly, longer the second potential plateau, which corresponds to HER, higher will be the parasitic reaction (HER) on the electrode. The length of first and second potential plateaus for 2^{nd}, 10^{th}, 40^{th}, 80^{th}, 120^{th}, 160^{th} and 180^{th} cycle are shown in Figure 7. The length of 1^{st} potential plateau in 2^{nd} cycle is about 48 mAh g^{-1} which increases gradually as formation proceeds. Its length reaches a maximum of about 390 mAh g^{-1} in the 180^{th} cycle. The length of second potential plateau gradually decreases with cycle number, which indicates suppression of hydrogen evolution on the electrode as formation cycles proceeds. The length of 2^{nd} potential plateau in 2^{nd} cycle is about 395 mAh g^{-1} which decreases gradually with charge/discharge cycles. A minimum length of about 60 mAh g^{-1} is observed in 180^{th} cycle.

Charge-potential profiles for carbonyl iron electrodes at the beginning of the charging in cycle number 1, 2, 4, 6, 8 and 10 are shown in Figure 10. An initial "potential overshoot" is observed at the onset of charge from 2^{nd} cycle onwards that gradually decreases as the formation proceeds. It is noteworthy that this "potential overshoot" is not observed during the first cycle charge. This "potential overshoot" is due to slow nucleation and resistance of the system towards the phase transformation, namely hexagonal $Fe(OH)_2$ to cubic α-Fe. The potential overshoot is not observed at the onset of first cycle charge, because $Fe(OH)_2$ may not be present in the as-prepared electrode. During the first cycle discharge, a significant amount of $Fe(OH)_2$ is formed on the electrode due to oxidation of α-Fe. In Figure 7, initial "potential overshoot" which is observed during second cycle charge is shown with a circle in the charge potential profile for carbonyl iron electrode. Similar potential overshoot at the onset of charging is observed in Li-ion battery materials like anatase TiO_2 and $LiFePO_4$, and sulphur in lithium-sulfur cells [36–40]. In the literature [36], it is reported that the initial potential overshoot for anatase TiO_2 is dependent on the specific surface area of the sample. Anatase TiO_2 with varying specific surface area was prepared and electrochemically studied and it is shown that the initial potential overshoot decreases as the specific surface area of the material increases. For carbonyl iron electrode, the "potential overshoot" gradually decreases as the formation cycle proceeds from cycle 2 onwards. This observation can be explained by considering the active surface area of $Fe(OH)_2$ in the discharged electrode, which increases progressively during further charge/discharge cycling due to the gradual penetration of electrolyte into the interior of the particles. The increase in the active surface area of $Fe(OH)_2$ with charge/discharge cycling in carbonyl iron electrode is clear from the observation that the length of the first potential plateau that corresponds to reduction of $Fe(OH)_2$ to α-Fe in the charge potential profile increases as the formation cycles proceed. As the active surface area for $Fe(OH)_2$ increases during formation cycles, the initial steep "potential overshoot" of about 20 mV observed during cycle 2 gradually broadens and becomes less pronounced as the formation cycles proceed limiting the magnitude of potential overshoot in cycle 10 to 5 mV.

Figure 11 shows the discharge potential profile for carbonyl iron electrode in cycle number 2, 10, 40, 80, 120, 160 and 180. The specific discharge capacity increases with cycle number since more amount of metallic iron is exposed to the electrolyte as the formation cycles proceeds. A maximum specific capacity of about 400 mAh g^{-1} is observed in 180^{th} cycle. Since the CIP has lesser surface area and porosity, it takes many charge/discharge cycles to reach the maximum specific capacity.

Figure 12 shows the discharge potential profile for carbonyl iron electrode at varying discharge rates, namely $C/10$, $C/5$, $C/2$, C and $2C$ rate. Specific discharge capacities of 420, 402 and 371 mAh g^{-1} are obtained at $C/10$, $C/5$ and $C/2$ rates with a faradaic efficiency of about 84, 80 and 74%, respectively. At higher discharge rates, namely

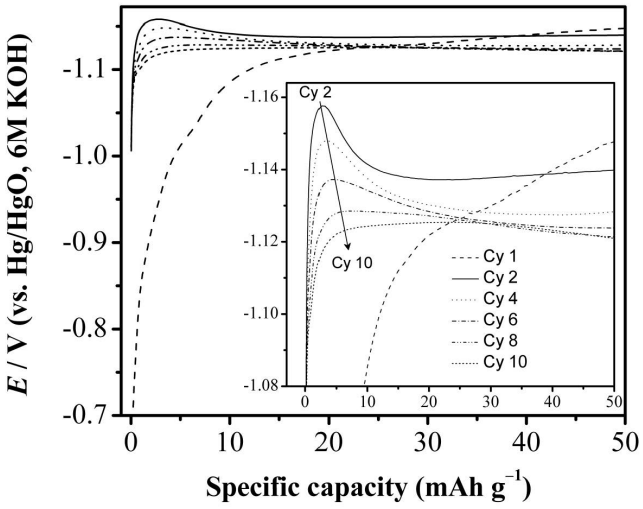

Figure 10: Charge-potential profiles for carbonyl iron electrode at the beginning of the charging for cycle number 1, 2, 4, 6, 8 and 10.

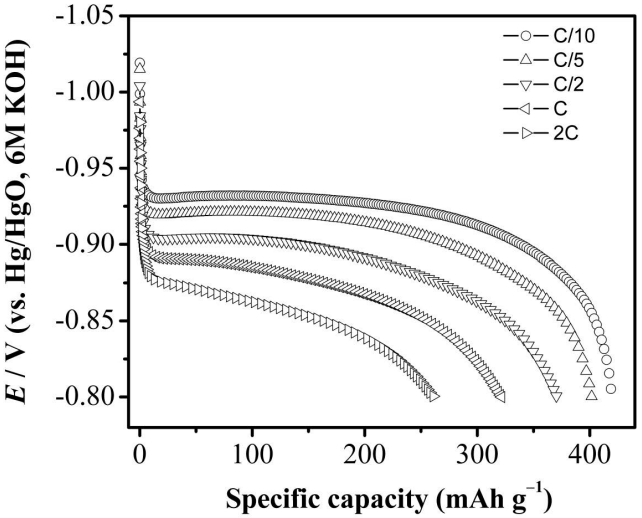

Figure 12: Specific discharge capacities for carbonyl iron electrode at varying discharge rates.

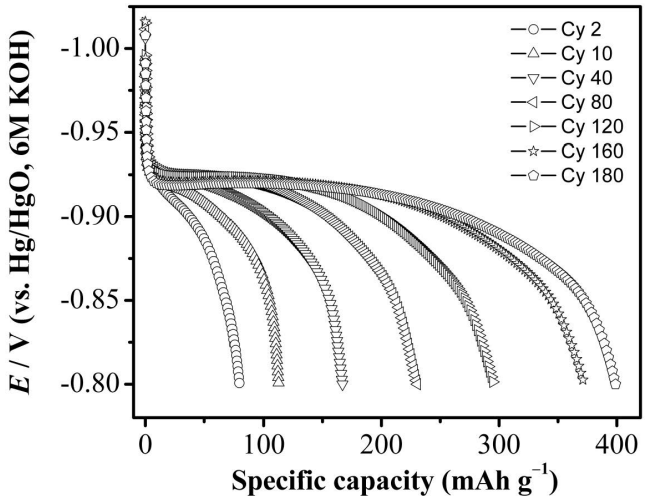

Figure 11: Discharge potential profiles for carbonyl iron electrodes during cycle number 2, 10, 40, 80, 120, 160 and 180 at a current density of 100 mA g^{-1}.

C and 2*C* rates, specific discharge capacities of about 321 and 261 mAh g^{-1} are obtained with a faradaic efficiency of 64 and 52%.

Figure 13 shows anodic steady state potentiostatic polarization for carbonyl iron electrode. Steady state potentiostatic polarization is carried out for a fully-formed electrode in fully charged condition (SOC ≈ 1), starting from −1.2 V to −0.8 V *vs.* MMO. The increase in the current at −1.2 V corresponds to hydrogen evolution on the iron electrode. As the electrode is polarized anodically, the current starts increasing from −0.95 V onwards and reaches a maximum at −0.86 V. On further polarization, the current decreases as the electrode becomes passive. The potential at which this phenomenon occurs is the passivation potential and the maximum current obtained is the critical passivation-current density (i_{crit}) that corresponds to 29 mA cm^{-2}.

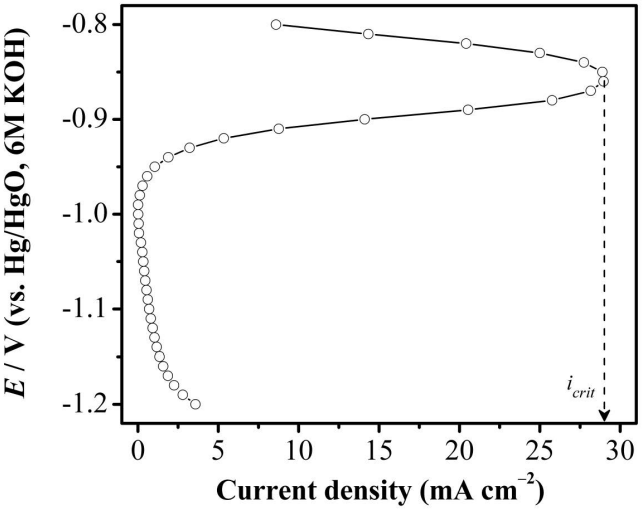

Figure 13: Anodic steady-state-potentiostatic-polarization data for carbonyl iron electrode.

A maximum specific discharge capacity of about 400 mAh g^{-1} is obtained for carbonyl iron electrode with a faradaic efficiency of about 80%. Due to the low specific surface-area of the CIP, the specific capacity increases gradually and it takes nearly 180 charge/discharge cycles to reach the maximum capacity value. As formation cycles

proceed, overpotential for reduction of $Fe(OH)_2$ to α-Fe decreases while overpotential for HER increases.

Acknowledgement: Financial support from Department of Science and Technology, Government of India and Indian Institute of Science, Bangalore under the Energy Storage System Initiative is gratefully acknowledged. KRP acknowledges beam time and travel support for XAFS experiments from RRCAT, Indore and help from Dr. S. N. Jha and Mr. Kapil Ingle in measurements.

References

[1] Ojefors L., Electrochim. Acta, 1976, **21**, 263-266.
[2] Ojefors L., Carlsson L., J. Power Sources, 1977/78, **2**, 287-296.
[3] Wang H., Liang Y., Gong M., Li Y., Chang W., Mefford T., et al., Nat. Commun., 2012, **3**, 917.
[4] Jayalakshmi N., Muralidharan V. S., J. Power Sources, 1990, **32**, 341-351.
[5] Chakkaravarthy C., Periasamy P., Jegannathan S., Vasu K. I., J. Power Sources, 1991, **35**, 21-35.
[6] Periasamy P., Babu B. R., Iyer S. V., J. Power Sources, 1996, **58**, 35-40.
[7] Huang K. C., Chou K. S., Electrochem. Commun., 2007, **9**, 1907-1912.
[8] Cerny J., Micka K., J. Power Sources, 1989, **25**, 111-122.
[9] Cerny J., Jindra J., Micka K., J. Power Sources, 1993, **45**, 267-279.
[10] Narayanan S. R., Surya Prakash G. K., Manohar A., Yang B., Malkhandi S., Kindler A., Solid State Ionics, 2012, **216**, 105-109.
[11] Manohar A. K., Malkhandi S., Yang B., Yang C., Surya Prakash G. K., Narayanan S. R., J. Electrochem. Soc., 2012, **159**(8), A1209-A1214.
[12] Malkhandi S., Yang B., Manohar A. K., Surya Prakash G. K., Narayanan S. R., J. Am. Chem. Soc., 2013, **135**, 347-353.
[13] Vijayamohanan K., Shukla A. K., Sathyanarayana S., J. Electroanal. Chem., 1990, **289**, 55-68.
[14] Vijayamohanan K., Shukla A. K., Sathyanarayana S., J. Power Sources, 1990, **32**, 329-339.
[15] Vijayamohanan K., Shukla A. K., Sathyanarayana S., J. Electroanal. Chem., 1990, **295**, 59-70.
[16] Balasubramanian T. S., Vijayamohanan K., Shukla A. K., J. Appl. Electrochem., 1993, **23**, 947-950.
[17] Balasubramanian T. S., Shukla A. K., J. Power Sources, 1993, **41**, 99-105.
[18] Shukla A. K., Ravikumar M. K., Balasubramanian T. S., J. Power Sources, 1994, **51**, 29-36.
[19] Ravikumar M. K., Balasubramanian T. S., Shukla A. K., J. Power Sources, 1995, **56**, 209-212.
[20] Caldas C. A., Lopes M. C., Carlos I. A., J. Power Sources, 1998, **74**, 108-112.
[21] Souza C. A. C., Carlos I. A., Lopes M., Finazzi G. A., de Almeida M. R. H., J. Power Sources, 2004, **132**, 288-290.
[22] Hang B. T., Eashira M., Watanabe I., Okada S., Yamaki J., Yoon S., et al., J. Power Sources, 2005, **143**, 256-264.
[23] Hang B. T., Watanabe T., Eashira M., Okada S., Yamaki J., Hata S., et al., J. Power Sources, 2005, **150**, 261-271.
[24] Hang B. T., Watanabe T., Egashira M., Watanabe I., Okada S., Yamaki J., J. Power Sources, 2006, **155**, 461-469.
[25] Hang B. T., Yoon S., Okada S., Yamaki J., J. Power Sources, 2007, **168**, 522-532.
[26] Kitamura H., Zhao L., Hang B. T., Okada S., Yamaki J., J. Electrochem. Soc., 2012, **159**(6), A720-A724.
[27] Egashira M., Kushizaki J., Yoshimoto N., Morita M., J. Power Sources, 2008, **183**, 399-402.
[28] Shukla A. K., Sampath S., Sundar Rajan A., Indian Patent Application no. 2177/CHE/2013.
[29] Rajan A. S., Sampath S., Shukla A. K., Energy Environ. Sci., 2014, **7**, 1110-1116.
[30] Ravel B., Newville M., J. Synchrotron Rad., 2005, **12**, 537-541.
[31] Zabinsky S. I., Rehr J. J., Ankudinov A., Albers R. C., Eller M. J., Phys. Rev. B, 1995, **52**, 2995-3009.
[32] Biesinger M. C., Payne B. P., Grosvenor A. P., Lau L. W. M., Gerson A. R., Smart R. St. C., Appl. Surf. Sci., 2011, **257**, 2717-2730.
[33] Manohar A. K., Yang C., Malkhandi S., Yang B., Surya Prakash G. K., Narayanan S. R., J. Electrochem. Soc., 2012, **159**(12), A2148-A2155.
[34] Pyper O., Hahn B., Schollhorn R., J. Mater. Chem., 1997, **7**(3), 465-469.
[35] Valyulene G., Zhelene A., Jasulaitene V., Shimkunaite B., Russian J. Appl. Chem., 2007, **80**(8), 1322-1326.
[36] Madej E., La Mantia F., Schuhmann W.,Ventosa E., Adv. Energy Mater., 2014, 1400829.
[37] Sasaki T., Ukyo Y., Novák P., Nat. Mater., 2013, **12**, 569-575.
[38] Meethong N., Shadow Huang H. Y., Speakman S. A., Carter W. C., Chiang Y. M., Adv. Funct. Mater., 2007, **17**, 1115-1123.
[39] Rosenman A., Elazari R., Salitra G., Aurbach D., Garsuch A., J. Electrochem. Soc., 2014, **161**(5), A657-A662.
[40] Zheng J., Gu M., Wang C., Zuo P., Koech P. K., Zhang J. G., et al., J. Electrochem. Soc., 2013, **160**(11), A1992-A1996.